Volume 15
Number 5
May 2022
Pages 1699–2166

Energy & Environmental Science

rsc.li/ees

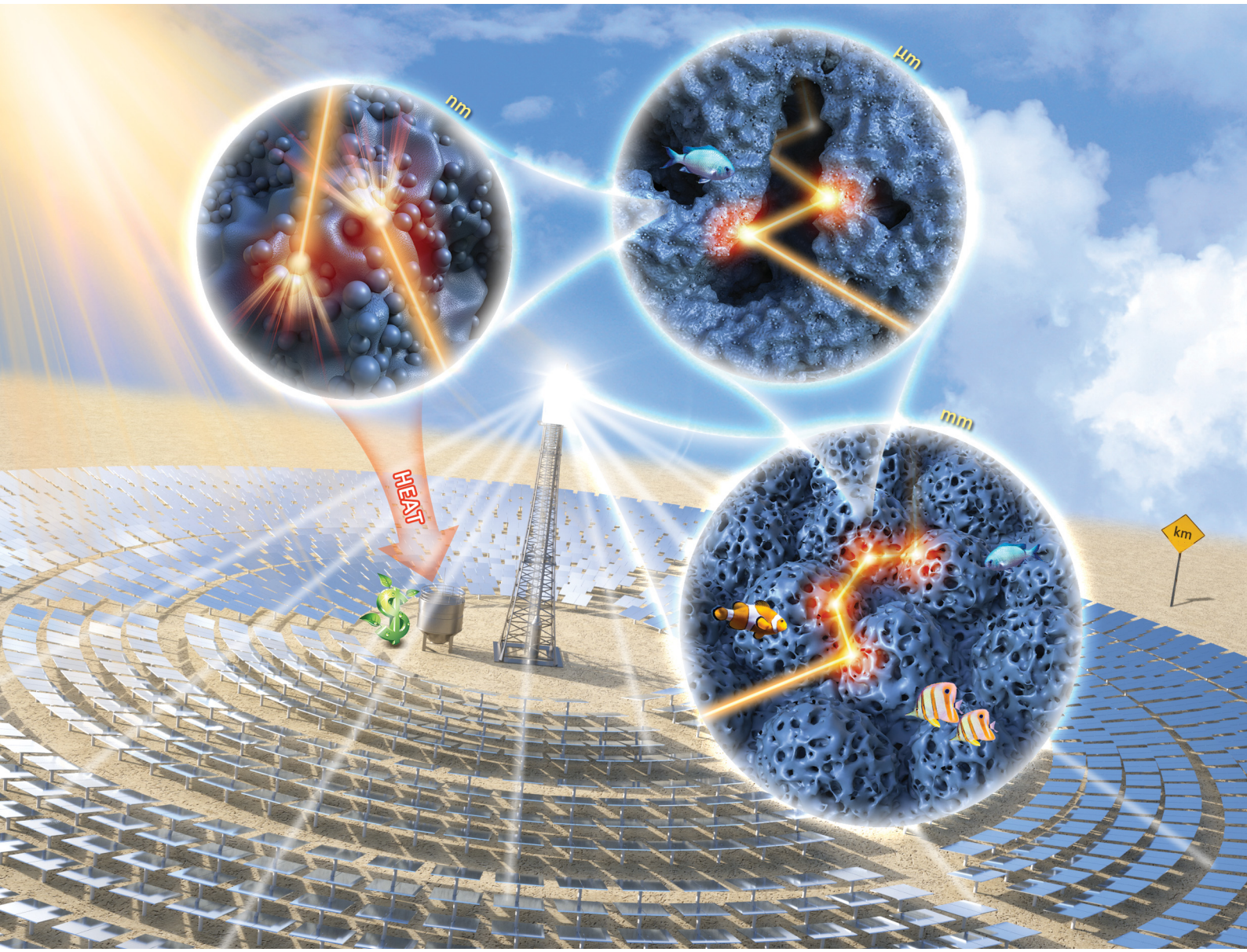

ISSN 1754-5706

ROYAL SOCIETY OF CHEMISTRY

PAPER
Juan F. Torres, Kaoru Tsuda, Joe Coventry *et al.*
Highly efficient and durable solar thermal energy harvesting *via* scalable hierarchical coatings inspired by stony corals

Energy & Environmental Science

ROYAL SOCIETY OF CHEMISTRY

PAPER

View Article Online
View Journal | View Issue

Cite this: *Energy Environ. Sci.*, 2022, **15**, 1893

Highly efficient and durable solar thermal energy harvesting *via* scalable hierarchical coatings inspired by stony corals†

Juan F. Torres, *[a] Kaoru Tsuda,*[b] Yasushi Murakami,[c] Yifan Guo, [a] Sahar Hosseini, [a] Charles-Alexis Asselineau, [a] Mahdiar Taheri, [a] Kurt Drewes,[d] Antonio Tricoli, [ef] Wojciech Lipiński [a] and Joe Coventry *[a]

Received 26th September 2021,
Accepted 9th March 2022

DOI: 10.1039/d1ee03028k

rsc.li/ees

Concentrating solar thermal (CST) is an efficient renewable energy technology with low-cost thermal energy storage. CST relies on wide-spectrum solar thermal absorbers that must withstand high temperatures (>600 °C) for many years, but state-of-the-art coatings have poor optical stability. Here, we show that the largely overlooked macro-scale morphology is key to enhancing both optical resilience and light trapping. Inspired by stony-coral morphology, we developed a hierarchical coating with three tuneable length-scale morphologies: nano- (~120 nm), micro- (~3 μm) and macro-scales (>50 μm). Our coating exhibits outstanding, stable solar absorptance of >97.75 ± 0.04% after ageing at 850 °C for more than 2000 hours. The scalability of our coating is demonstrated on a commercial solar thermal receiver, paving the way for more reliable high-performance solar thermal systems.

Broader context

The impact of anthropogenic climate change is being experienced across the globe. Renewable energy technologies are widely regarded as key to reducing greenhouse gas emissions and thus mitigating the devastating effects of climate change. Concentrating solar thermal (CST) is an important technology in that mix, owing to its low-cost thermal energy storage that can be used to drive many essential processes, from electricity generation to steel production. Vital to the wide adoption of CST is achieving high stability and efficiency of its photo-thermal energy conversion process, which generally occurs on a solar absorber coating. However, due to the extreme operation conditions of high-temperature and high-flux, state-of-the-art coatings degrade in performance rapidly, and often fail completely. Here, inspired by stony coral morphology, we report a hierarchical coating that incorporates advances in materials design and architecture to mitigate coating degradation and increase photo-thermal energy conversion. Our coral-inspired coating demonstrates ultra-high stability after ageing in air at elevated temperatures (≥800 °C), and has the highest reported sunlight absorptance. We show that the coating is scalable on commercial receivers and yields a significant improvement in photo-thermal efficiency for large-scale CST power plants. This work paves the way for more reliable high-performance solar thermal systems.

Introduction

Scleractinia, commonly known as stony corals (Fig. 1a), have evolved their morphology over millions of years to improve their chances of survival. A symbiotic relationship with algae, which need sunlight for photosynthesis, was an evolutionary milestone 240 million years ago that enabled corals to secure nutrients in otherwise infertile waters[1] and thrive in all Earth's oceans. Sunlight attenuation in seawater initially restricted coral colonies to shallow waters.[2,3] To thrive in deeper waters where light is more scarce, coral morphology[4] has evolved to improve light trapping[5] *via* multiple internal light reflections (Fig. 1b and c). We can then learn from stony-coral morphology in engineering and science where light trapping is needed, including sunlight harvesting using concentrating solar thermal (CST) systems.[6,7] Absorber coatings applied to solar receivers in CST plants have the function of converting concentrated sunlight in a wide-spectrum into thermal energy[8] for many applications, including electric power generation (Fig. 1d).[9,10] Importantly, CST incorporates thermal energy storage, a more affordable, scalable, and durable alternative than other well-known storage technologies for long duration energy storage.[11]

[a] College of Engineering and Computer Science, Australian National University, Canberra, Australia. E-mail: felipe.torres@anu.edu.au, joe.coventry@anu.edu.au
[b] Nano Frontier Technology, Tokyo, Japan. E-mail: kaoru.tsuda@nano-frontier.com
[c] Faculty of Textile Science and Technology, Shinshu University, Ueda, Japan
[d] Vast Solar, Sydney, Australia
[e] College of Science, Australian National University, Canberra, Australia
[f] Faculty of Engineering, University of Sydney, Sydney, Australia
† Electronic supplementary information (ESI) available. See DOI: 10.1039/d1ee03028k

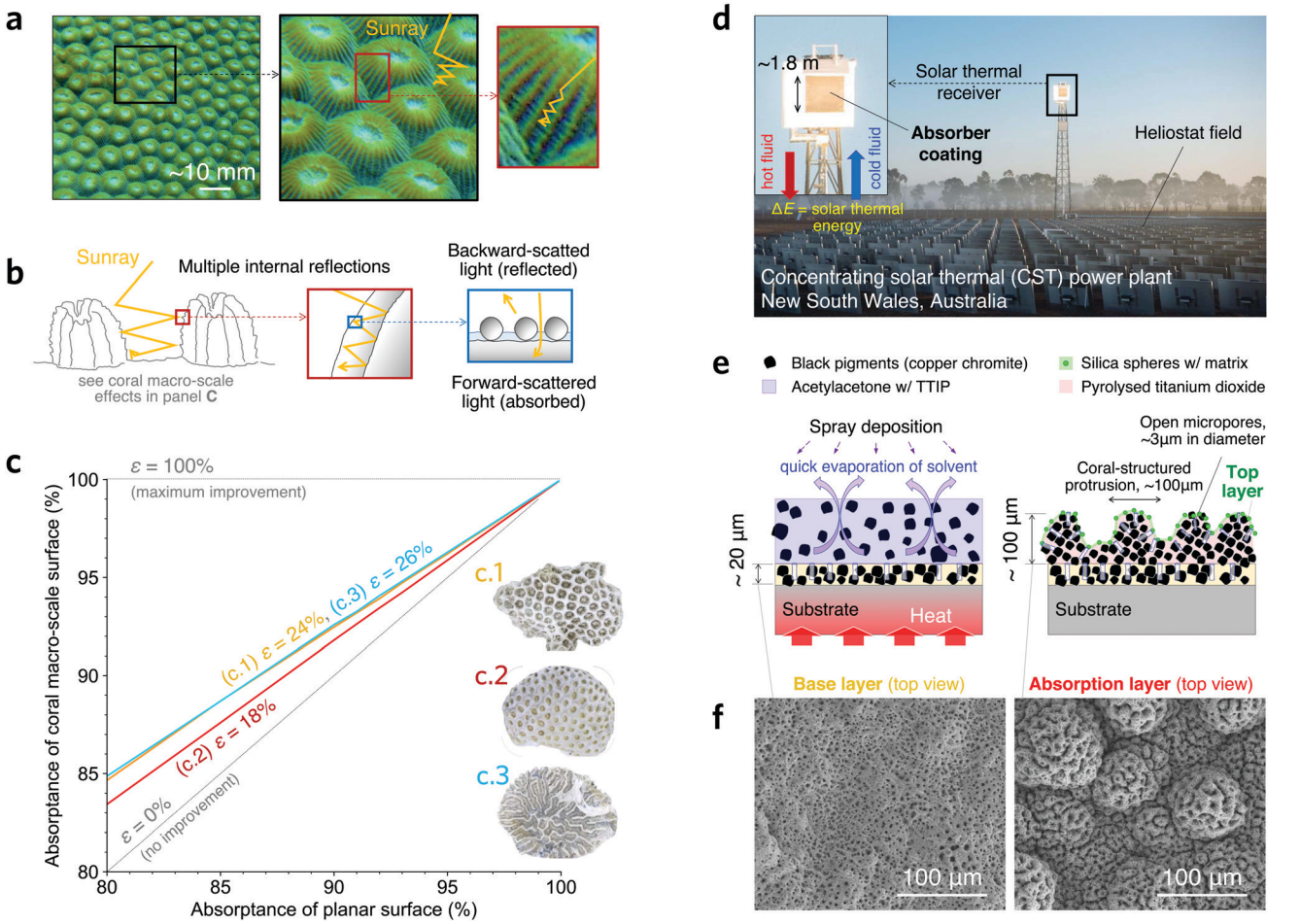

Fig. 1 A coral-inspired high-temperature solar absorber coating. (a) Photo of a common stony coral (genus *Montastraea*) showing lumpy macro-scale protrusions with smaller features (see other stony coral species in Fig. S1a–c, ESI†). Light trapping is improved *via* multiple internal reflections. (b) Schematic illustrating the different optical interactions occurring within a hierarchical coral structure; the light–matter interaction for the smaller length-scale features results in forward and backward scattering. (c) Ray-tracing simulation results showing the increment of absorptance in three coral macro-scale morphologies when applying a planar surface absorptance; the effectiveness ε in reducing reflection loss (see definition in Methods) for each morphology is indicated and independent of the planar surface absorptance. Insets show photos of modelled coral morphologies; an example of surface analysis is shown in Fig. S1d–f (ESI†). (d) CST power plant of Vast Solar in Australia where the scalability of the proposed coating is demonstrated on a commercial solar thermal receiver (inset). (e) Proposed coating having a ~20 μm thick base layer with open micropores of ~3 μm in diameter, an absorption layer having lumps of >50 μm in diameter resembling corallites in scleractinias, and a top layer with silica matrix and spheres of ~120 nm in diameter. (f) Scanning electron microscopy (SEM) images of the base (left) and the absorption (right) layers.

A key barrier to the wide adoption of CST, contributing to both increasing cost and reducing performance, is the poor durability of its light-absorbing coatings.[12] These coatings need to withstand high temperatures (>600 °C) and thousands of thermal cycles over many years of operation.[13] The most widely used CST coatings are spinel-based coatings (Note 1, ESI†) such as Pyromark 2500® (henceforth referred to as Pyromark),[14] which is considered the gold-standard in the CST industry. These coatings implement an organic binder[15] that decomposes during a curing process to produce a nano-textured porous coating with spinel pigments, without macro-scale (>50 μm) features. Solar absorptance, the key performance metric,[12,16] is typically reported after long-term isothermal exposure at high temperature, with the highest reported values being 94.6% after ageing for 2350 h at 850 °C,[14] 97.2% after ageing for 2000 h at 800 °C,[15] and 96.3% after ageing for 3800 h at 770 °C.[13] However, unstable optical performance is generally observed in CST coatings because the elevated temperatures re-arrange the material phases,[17] alter the material composition,[12,13] modify the nano-scale morphology *via* sintering and crystal grain growth,[18] and may change large-scale morphological features due to the growth of an oxide layer between the coating and metallic substrate,[13] *e.g.* by peeling off. Advanced sunlight absorbers made of carbon nanotubes[19] and graphene[20] can absorb more than 99% of solar irradiation from every angle, but these coatings burn at the surface temperatures commonly found in conventional receivers.[21]

Most coating research so far has focused on texturing the nano-scale morphology and improving the thermal stability of the materials,[12–15,22–24] while neglecting the micro- (~3 μm)

and macro-scale (>50 μm) geometries[25] and the tuning of various length-scale morphologies in the coating to maximise light absorptance. State-of-the-art surface texturing methods in CST coatings include the use of sacrificial beads with pre-selected sizes that burn during curing, thus introducing the desired microporosity in the coating,[15,26,27] and photolithography-based methods that can yield highly accurate surface morphologies.[12,28] However, methods based on sacrificial beads often lead to highly porous coatings that may weaken their mechanical strength. Photolithography-based methods can produce highly dense layers with micro-textured morphology, but the scalability is a major issue due to the vacuum requirements for deposition on tubes larger than 3 m.[28] Solar thermal receivers with tube lengths larger than 10 m are common in the industry.[29] Besides, these methods have largely focused on introducing spectral selectivity, *i.e.* increasing solar absorption in the visible range while reducing thermal emission in the infrared range (Kirchhoff's law states the equivalence between spectral absorptance and emittance). However, it has been reported that for high-flux high-temperature applications, highly absorptive coatings can achieve the same or even better performance than spectrally selective ones.[30,31] Therefore, in this work, we focus on increasing the sunlight absorptance of the coating (before and after ageing) for the entire wavelength spectrum *via* multi-length scale light trapping to maximise photo-thermal energy conversion, even if there is a penalty due to thermal emission.

Furthermore, all CST-based electric power generation—which is the targeted application of our coating—has working temperatures below 800 °C.[9] Even for high-performance solar thermal receivers using liquid sodium as heat transfer fluid,[32] the peak absorber surface temperature has been reported to be approximately 830 °C. Hence, the targeted temperature application of our coating is below 850 °C. Note that larger temperatures can be tested to accelerate the degradation. Improvement of receiver coatings for such large temperatures has been identified as one of the top priorities in the CST community.[33] High-temperature solar absorbers that can withstand temperatures above 1300 °C have been developed,[34] but these are limited to special corrosive-resistance substrates with a similar thermal expansion coefficient to the coating. These types of substrates are yet to be adopted in the CST industry due to their inferior strength compared to superalloys. For the absorber coating to have a tangible impact on CST technologies, the tested substrate should be a material that can withstand high peak fluxes and thermal stresses, such as iron- or nickel-based alloys (*e.g.* stainless steel and Inconel).

Hierarchical structures have been shown to be a powerful tool to improve radiative cooling in clothing,[35] as well as mechanical rigidity and stability in sea sponges.[36] Here, we show that a hierarchical design with coral-inspired micro- and macro-scale features can produce high-temperature solar absorbers with enhanced light absorption and outstanding optical resilience, which we define as the capacity to retain stable optical properties despite material degradation.

Results and discussion

Coral-inspired coating with hierarchical light-trapping structure

A hierarchical light-trapping coating is developed with three length-scale morphologies: nano- (~120 nm), micro- (~3 μm), and a macro-scale (>50 μm). Our proposed hierarchical structure has a large hierarchical range with a ratio of largest to smallest length-scale feature of *ca.* 800, which is in stark contrast with the only other theoretically proposed bio-inspired hierarchical absorber for CST[37] whose ratio is *ca.* 3. A wide-range multi-length scale morphology can be key to enhancing sunlight absorption and optical resilience. To explore the benefits of the coral-structured morphology, we model the improvement of light trapping in three species of stony corals. Simulation results (Fig. 1c) show that the analysed coral morphologies reduce the reflection loss by 18–26% (see definition of effectiveness in Methods), while exhibiting an intrinsic optical resilience. That is, even if the absorptance of the flat surface decreases (horizontal axis in Fig. 1c), it is compensated by multiple light reflections at the macro-scale level in the coral structure (Fig. 1b) as evidenced by the increased absorptance (vertical axis). In contrast to nano-scale features that are more susceptible to change under high temperature, micro- and macro-scale features are mostly unaffected. Multi-length scale design of a light-absorbing coating including macro-scale features has not been reported in the CST literature. In addition to light trapping, such a morphology could have other benefits including mechanical strength improvement and drag reduction (see Note 2, ESI†).

The proposed coating has a novel three-layer structure comprised of a base layer, an absorption layer, and a top layer (Fig. 1e), each having a contribution to both light absorptance and durability. The base and absorption layers contain black spinel pigments ($Cu_{0.64}Cr_{1.51}Mn_{0.85}O_4$) bonded by alumina ($Al_2O_3$) and titania ($TiO_2$), respectively. Regarding the contributions to absorptance, the base layer has open micropores with light-trapping features, such as in the coral of Fig. 1c.1. The absorption layer exhibits a self-assembled morphology with macro-scale protrusions, such as the coral in Fig. 1c.2, having the same open micropores as the base layer. Hence, both micro- and macro-scale morphologies can introduce the intrinsic optical resilience observed in stony corals. The top layer is a nano-textured surface that contributes to light absorption *via* enhanced forward scattering and optical resonance[38,39] induced by ~120 nm silica nanospheres and a ~8 nm matrix (Fig. S3–S6, ESI†). Regarding the contributions to durability, the base layer helps mitigate coating delamination because the alumina binder adheres well to the substrate while the open micropores produce disjoint features that prevent the propagation of local failures. The absorption layer is comprised of a robust and dense titania binder (Fig. S7, ESI†). The chromium-based spinels in both base and absorption layers contribute to the formation of a thick substrate-protecting chromium oxide layer (Fig. S7, ESI†).[13] The silica matrix in the top layer is thought to help prevent pigment loss after crystal grain growth.

The proposed coating is made *via* a simple and scalable deposition process (Fig. 1e) that yields tuneable length-scale

morphologies. Our coating uses commercially available materials and processes that are easily accessible, without a significant cost increase compared to conventional CST coatings (see Note 2 for comments on cost benefits, ESI†). A matrix with open micropores in both the base and absorption layers (Fig. 1f) is formed by three sequential events during the solution deposition onto a substrate held at ~300 °C: (1) desorption of the solvent (ligand) coordinated to Al and Ti, (2) quick evaporation of the desorbed solvent, resulting in the formation of open micropores, and (3) thermal decomposition (pyrolysis) of Al and Ti (from the desorbed solvent), resulting in a matrix composed of alumina (base layer) or titania (absorption layer) strongly bonding the black pigments (see more details in Methods). The coral-inspired micro- and macro-scale morphologies in the absorption layer are tuned through a careful combination of factors including pyrolysis and solvent evaporation rates (more details shown in Fig. S14–S16, ESI†), resulting in a robust and repeatable coral-like structure (Fig. 2a) composed of titania-bonding black spinel pigments. Importantly, the oxide binders do not exhibit the nanopores found in

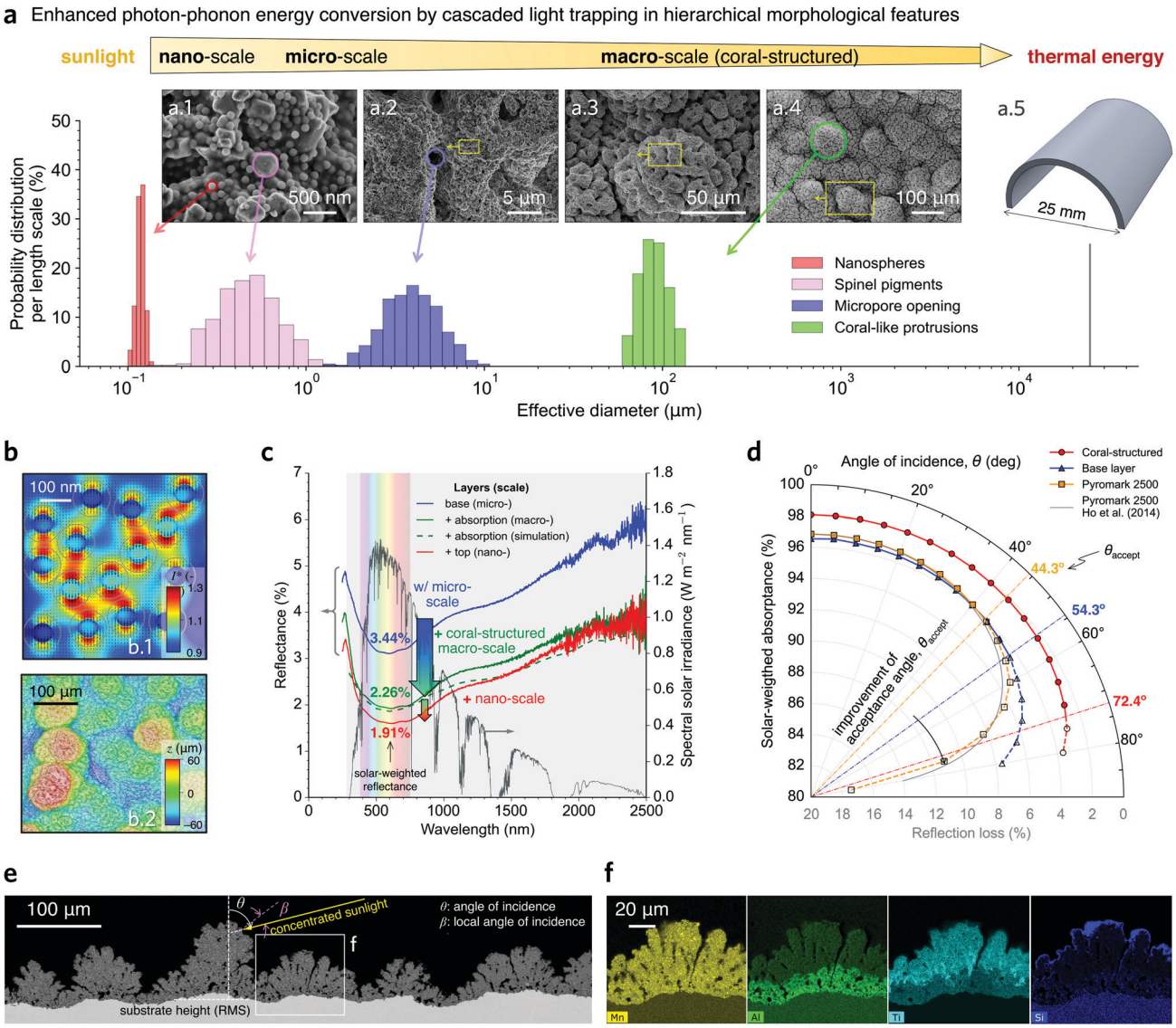

Fig. 2 Characterisation of the hierarchical coral-structured coating. (a) Histogram of effective diameter for the hierarchical morphological features in our coating in terms of the probability distribution per length scale. SEM images showing nanospheres and pigments (a.1), coral-inspired open micropores (a.2 and a.3) and macro-scale protrusions (a.3 and a.4). The tubes of the receiver are included (a.5) for reference. (b) Simulation results showing the magnitude of the sunlight that is forward scattered below the nanospheres (top) (details in Fig. S5 and S6, ESI†); a section of the three-dimensional scan of the coating topography (bottom) used in the ray-tracing simulations. (c) Reflectance (left axis) as a function of wavelength showing the reduction in reflectance as each layer is added in the deposition process; the green dashed line indicates the ray-tracing simulation results. (d) Solar-weighted absorptance and reflection loss as a function of the angle of incidence θ; the coral-structured morphology significantly increases the acceptance angle θ_{accept}. (e) Back-scattered electron (BSE) image of the cross-sectioned pristine sample; an arbitrary θ is shown. (f) Elemental mapping of the magnified cross-sectioned region indicated in panel (e) for the black pigment (Mn) and three other elements that are mostly present in the base (Al), absorption (Ti), and top (Si) layers (more details in Note 3, ESI†).

most CST coatings, *e.g.* ref. 13, 15, 22 and 27, promoting a strong bonding to black pigments (Fig. S7, ESI†) while the nano-scale texture is accurately tuned by the top layer (Fig. 2a.1).

The excellent light-trapping effect of hierarchical structures has been investigated in various fields, *e.g.* in hierarchical porous materials for catalytic applications[40] and photo-electro-chemical[41] and water splitting[42] cells. A consensus on structural design is that the size of hierarchical structure should be a trade-off between light absorption and other factors, such as charge transport and mass transfer in photovoltaic cells. Hence, oversized nanostructures are usually avoided even if they showcase greater light absorption. In CST, control strategies are generally adopted to keep the heat transfer fluid (HTF) at a stable outlet temperature, *e.g.* by varying its flow rate. The coating thickness is potentially a constraint because, if overly thick, it may increase the thermal barrier of the receiver external surface, which translates into a large temperature difference through the thickness of the coating from the air–coating (hotter) to the coating–substrate (colder) boundaries. As the HTF is kept at relatively constant temperature, this large temperature difference could potentially lead to excessive thermal losses—both convective and radiative[43]—due to the elevated temperature on the external coating surface exposed to the ambient air. We modelled a full-scale CST power plant (Note 6, ESI†) considering detailed tubular features of the receiver, and we estimate that the coating effective thickness should be kept below about 200 μm (Note 7, ESI†) to avoid unrealistically high temperature values. We also found that the effect on receiver thermal efficiency when the coating thickness is less than 40 μm (Note 7, ESI†) is minor, where 40 μm is representative of the thickness of our coral-structured coating. Although the thermal barrier also depends on the thermal conductivity of the coating, our modelling results show that thermal conductivity within values reported in the literature[44] (between 0.8 and 6 Wm^{-1} K^{-1}) had a minimal impact on the receiver thermal efficiency (Note 7, ESI†).

Cascaded light-trapping mechanisms from hierarchical features

In CST technologies, photons from the sun are optically concentrated, often beyond 1000 times, onto the surface of a receiver coated with a light-absorbing coating. These photons first interact with small length-scale features in the coating (*e.g.* nanospheres), which reflect (or re-emit) photons in a wide wavelength range. Importantly, some of these photons can be intercepted by large length-scale features (*e.g.* coral-like protrusions) to be re-absorbed in a ''cascaded light trapping'' process. The important length-scales featured in our coating are shown in Fig. 2a: the nano- (a.1), micro- (a.2), and macro- (a.3 and a.4) scales. Cascaded light trapping ensures that a drop in effective absorptance is mitigated if a length-scale feature has degraded. For example, when mechanically peeling off the macro-scale protrusion in our coating, the benefits of the micro-scale porosity are still evidenced by a large spectral absorptance (Fig. S25, ESI†). Similarly, we found that the macro-scale features without micropores still exhibits excellent light-trapping properties (Fig. S14a, ESI†). Micropores could disappear due to soiling with particulate matter, such as penetration of PM2.5, and their subsequent annealing at high temperatures. In contrast, because PM2.5 is much smaller than the macro-scale features, this particulate matter is less susceptible to getting trapped in between macro-scale protrusions.

Computational electromagnetics simulations of the top layer indicate that both forward scattering and backscattering of sunlight occur for wavelengths in the visible range. Although backscattering reduces the light absorption, forward scattering creates regions of high intensity underneath the silica nanospheres (Fig. 2b.1). This local nano-scale concentration of forward scattered sunlight increases absorption by a larger amount than the energy lost *via* backscattering for most of the wavelength range (Fig. S6, ESI†). Our simulations also show that the intensity of the forward scattered light becomes larger underneath the narrow gaps between nanospheres (Fig. 2b.1) due to a resonance effect, also observed in surface plasmons[24] for thin-film solar cells.[45] For a densely packed arrangement of silica nanospheres (surface coverage ratio of 47%), simulations show that this resonance effect intensifies for nanospheres with a diameter of 124 nm (Fig. S6, ESI†). Experimentally, we applied a top layer with nanospheres having a nominal diameter of 10 and 50 nm and measured an inferior absorptance enhancement in the hierarchical structure compared with the case of 100 nm (124 nm in effective diameter; Fig. S3, ESI†). Therefore, our simulation and experimental results indicate that a highly dense layer of silica nanospheres with a diameter of approximately 120 nm reduces sunlight reflection (Fig. S3–S6, ESI†). The measured spectral reflectance is reduced throughout the entire spectrum when the top layer is deposited last (red line in Fig. 2c), while the solar-weighted reflectance is reduced from 2.26% (without the top layer) to 1.91% (with the top layer), *i.e.* by 15.6% (relative value). Hence, we demonstrate that the use of nanospheres is an effective way of introducing a nano-texture on the coating external surface without having extensive nano-porosity[26,27] within the coating that could compromise its durability.[13] Ageing tests at 900 °C for 1000 h (Fig. S4, ESI†), however, reveal that a top layer with an excessive amount of nanospheres worsens their adhesive strength and decreases light trapping after ageing. Hence, the post-ageing solar absorptance is optimised by tuning the nanosphere diameter and number density, based on extensive thermal ageing results (*e.g.* Fig. S4, ESI†).

In addition to the multiple reflections between the macro-scale protrusions, light is also trapped by multiple reflections within the micropores. Note, however, that the micropore density is kept moderate (Fig. 2a.2), as a large pore number per surface area could worsen the mechanical robustness of the coating.[23] Monte Carlo ray-tracing simulations show that multiple reflections between macro-scale protrusions increase light absorption and agree well with the measurements (Fig. 2c green lines). Importantly, a significant improvement in absorptance is obtained throughout the entire wavelength spectrum, as the improvement brought by the macro-length scale is purely

geometrical and therefore wavelength independent. The solar-weighted reflectance is significantly reduced from 3.44% (base layer) to 2.26% (with the absorption layer, but without the top layer), *i.e.* by 34.3% (relative value).

Furthermore, we found that introducing micro- and macro-scale features significantly improves the light acceptance angle θ_{accept} of the coating (Fig. 2d and Fig. S8, ESI†), from 44.3° for Pyromark (which has a rather flat morphology) to 72.4° for our coral-structured coating. θ_{accept} is defined here as the angle of incidence for which the solar-weighted hemispherical reflectance increases by 1% (or absorptance reduces by 1%) relative to the normal-incidence hemispherical reflectance (or absorptance). A larger acceptance angle means that the coating can absorb more solar irradiation at the steep incidence angles typical in non-planar receiver geometries, irradiated from many directions. Using our definition, Pyromark has an acceptance angle of $\theta_{accept} = 44.3°$. We show that the micropores in the base layer (without coral-like protrusions or the top layer) yield $\theta_{accept} = 54.3°$, while the coral-like protrusions in the absorption layer greatly increase its value to 72.4°. For the maximum measurable angle of 80°, the solar-weighted absorptance only decreases by 1.7% from the normal-incidence value, whereas for Pyromark it decreases by 14.7%. Cross-section scanning electron microscopy (SEM) measurements (Fig. 2e) reveal that light at high incidence angles is intercepted by the coral-like protrusions, suggesting two contributing factors to the large θ_{accept}: first, the local angle of incidence β is closer to normal incidence, which is expected to have higher absorptance than for high values of β (based on Fresnel equations); second, a portion of the reflected light from the protrusion is re-absorbed by the coating (multiple reflections, as in Fig. 1b). The cross-section SEM also shows that the open micropores have an elongated morphology penetrating most of the coating. Cross-section energy-dispersive X-ray spectroscopy (EDS) results (Fig. 2f, Note 3, ESI†) highlight the presence of black spinel pigments (containing Mn) throughout the bulk of the coating, while the base, absorption, and top layers contain bonding oxides of Al, Ti, and Si, respectively.

Characterisation of long-term thermal stability and degradation

The absorptance of our coating is first compared with Pyromark for both spectral and solar-weighted absorptance values (Fig. 3a and b), before and after ageing at 800 °C for up to 3000 h, and thermal cycling tests up to 3000 cycles. In pristine condition, the coral-structured coating has higher spectral absorptance than Pyromark for most wavelengths beyond 350 nm. After ageing, the coral-structured coating has a significantly higher spectral absorptance than Pyromark, reducing the solar-weighted reflection loss by 37%. Prior to the long-term ageing tests, we conducted shorter-term ($\leq$100 h) isothermal ageing ($\leq$850 °C) with two substrates used in CST applications (Note 4, ESI†), as the substrate is a determining factor in the durability of the coating.[14,34] The coral-structured coating was found to be highly stable on both substrates with a high solar-weighted absorptance (>97.3% for the preliminary macro-scale morphology in Fig. 3f).

Long-term testing (Fig. 3b) shows that the coral-structured coating has superior optical stability in comparison to our measurements of Pyromark, and the results of others from two of the best performing long-term stable coatings.[13,15] The thermal cycling (Fig. 3b inset) follows a cycle-and-hold pattern (Fig. S9, ESI†), which we previously found to be more stringent than rapid cycling tests.[18] Cross-section EDS results show that the coating morphology is largely unchanged (Fig. 3c) despite the growth of an underlying oxide layer (Note 3, ESI†). The thermal cycling tests yield a slightly lower solar-weighted absorptance than the isothermal tests with the same hold time at 800 °C, but still our coating exhibits an outstanding absorptance greater than 97.5% after 3000 cycles (Fig. 3b inset, Fig. S9, S10, ESI†). Our ray-tracing modelling (*e.g.* Fig. 2c) and experimental results (Fig. 3b) suggest that the multiple reflections within the coral structure are responsible for the observed optical resilience and significantly lower reflection loss. Furthermore, measurements of the spectral near-normal emittance (Fig. 3d) are used to estimate the temperature dependant total hemispherical emittance (Fig. S11, ESI†), revealing that our coating is much more optically stable in the infrared spectrum than Pyromark.

Coral-structured coatings with a preliminary macro-scale morphology (Fig. 3f) were aged at 850 °C, and shown to be optically stable (Fig. 3e, green data points), keeping their average solar-weighted absorptance >96.0% even after 4000 h exposure on both a nickel-based alloy and a stainless steel (Fig. S12, ESI†). The morphology was further improved by increasing the number and size of the macro-scale protrusions (Fig. 3f), which produced an ultra-stable solar-weighted absorptance of 97.75 ± 0.04% (average ± standard deviation) between 200 h and 2000 h (*i.e.* 8.3 and 83 days) when aged at 850 °C (Fig. 3e blue data points). Furthermore, the top layer improved the absorptance by more than 1% after ageing at 900 °C (Fig. 3e inset), whereas an improvement up to 0.4% was observed in the pristine condition (Fig. S4, ESI†). These results demonstrate that different length-scale features can be tuned to optimise light absorption (Fig. S4 and S14–S16, ESI†). Under isothermal ageing at 900 °C, the coral-structured coating was not as stable as for ≤850 °C, following a quasi-linear decrease in solar-weighted absorptance (Fig. 3e) that is associated with the widening of cracks and peeled off regions at discrete locations (Fig. 4a).

In general, wet-spray deposition coatings are porous because, after deposition at room temperature, the organic binder is decomposed during curing resulting in pores.[13] This porosity may reduce the mechanical strength of the coating. In contrast, the proposed coating deposition method with the substrate held at ~300 °C forms highly-dense thermally-decomposed oxides bonding chromium-based spinel pigments. This configuration yields a significant improvement in durability due to the strength of the titania binder in the absorption layer (Fig. S7, ESI†). Furthermore, a thicker protective chromium oxide layer generated by the presence of

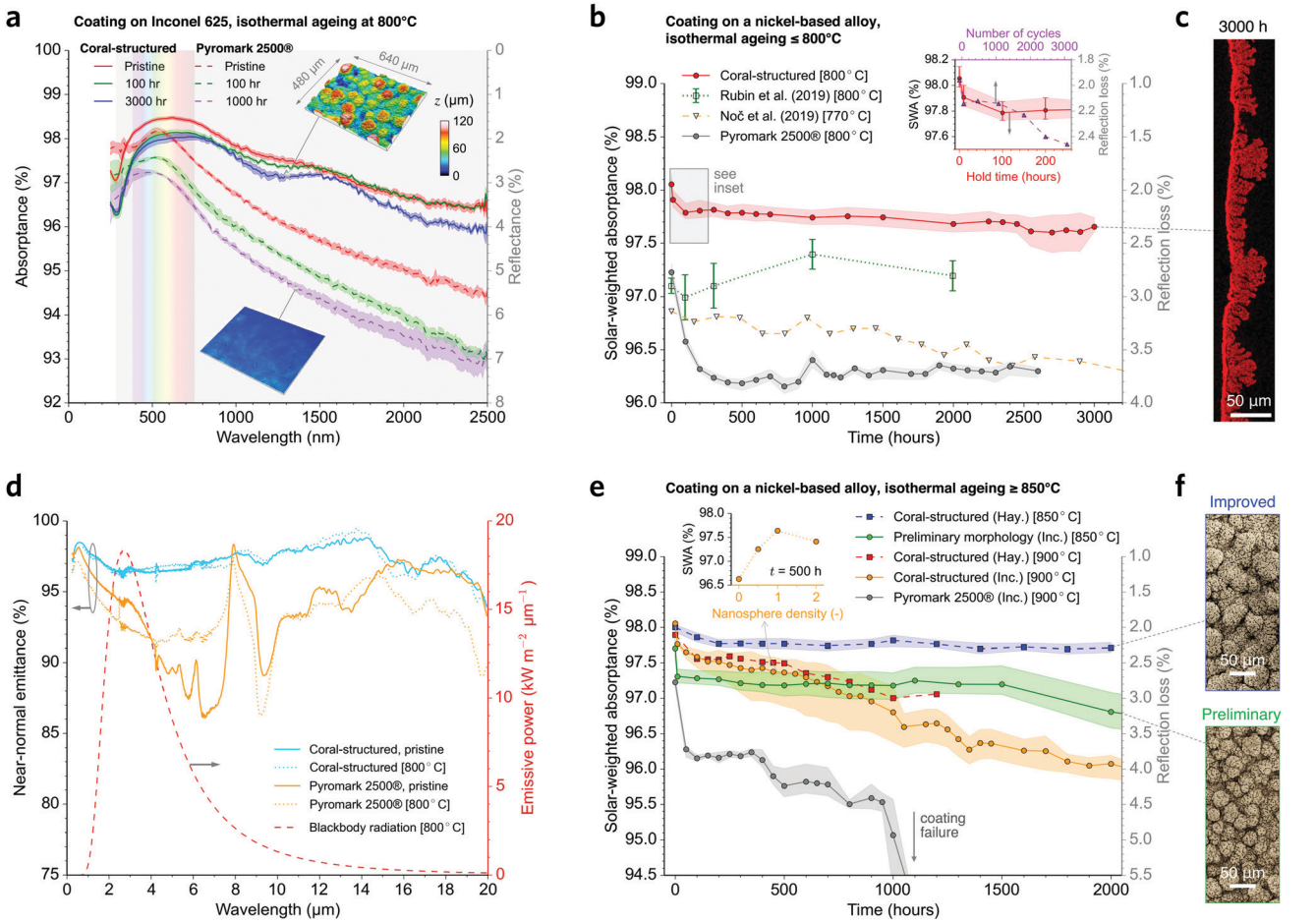

Fig. 3 Comparison of the proposed coating with the state-of-the-art. (a) Spectral absorptance (reflectance on right axis) for the proposed coral-structured coating and improved Pyromark 2500® (gold-standard) on Inconel 625. The insets show the macro-scale morphologies. (b) Solar-weighted absorptance (SWA; left axis) as a function of isothermal annealing time at $\leq$800 °C for our coating and three different coatings: our Pyromark coating and two best performing coatings in the literature[13,15] (ageing temperature indicated in brackets in the legend); the coral-structured coating yields a superior stability and light absorption. The inset shows the results for a cycle-and-hold test[18] compared with isothermal results at equivalent hold time (Fig. S9 and S10, ESI†). (c) Cross-section elemental mapping of oxygen after ageing at 800 °C for 3000 h, showing an intact coral-structured morphology. (d) Spectral near-normal emittance including the infrared range spectrum, showing the good stability of our coating (see Fig. S11 for the temperature-dependence of the total hemispherical emittance, ESI†). (e) Solar-weighted absorptance as a function of isothermal annealing time at $\geq$850 °C for two nickel-based alloys: Haynes 230 (Hay.) and Inconel 625 (Inc.); see Fig. S12 (ESI†) for results with stainless steel. The inset shows the effect of nanosphere number density on the absorptance after ageing at 900 °C for 500 h. See more details in Fig. S4 (ESI†). (f) SEM images showing the improved (top) and preliminary (bottom) macro-scale morphologies.

chromium-based spinel pigments (Fig. S7, ESI†) reduces spallation risks, contributing to the coating durability.[46] After extensive thermal annealing at 850 °C, however, we observe that the oxide binder density is significantly reduced, degrading the internal nano-scale morphology (Fig. S26, ESI†), possibly due to cation diffusion at elevated temperatures (Note 3, ESI†).[17,47] The reduction in oxide binder density is thought to have contributed to mechanically weakening the coating (Fig. S7 and S25, ESI†).

The three-layer approach enables functional design of each individual layer: the base layer provides adhesion, the absorption layer provides optical resilience and improves the substrate-protecting chromium oxide layer, and the top layer provides light absorption improvements. Importantly, disjoint features were observed to prevent propagation of delaminated local regions in the coating (Fig. 4a). The result is a coating that is delamination-resistant and has a higher absorptance than nanoporous coatings, *e.g.* ref. 13–15. Under isothermal annealing at 900 °C, the nano-scale morphology on the coating surface was largely retained (Fig. 4a.3 and Fig. S20d, ESI†), despite changes in the nano-scale morphology within the absorption layer (Fig. S26, ESI†). Cross-section EDS results (Fig. 4b) show the ageing process for the coating on an Inconel 625 substrate at 800 °C (more details on other substrates and temperatures in Note 3, ESI†). The mostly unchanged X-ray diffractometry (XRD) patterns provide further evidence of coating stability at high temperatures (Fig. 4c and Fig. S17, ESI†). Prior to the scalability tests, coral-structured coating samples were placed in a high-flux environment in the spillage region of a solar thermal receiver at a pilot CST power plant for up to six months

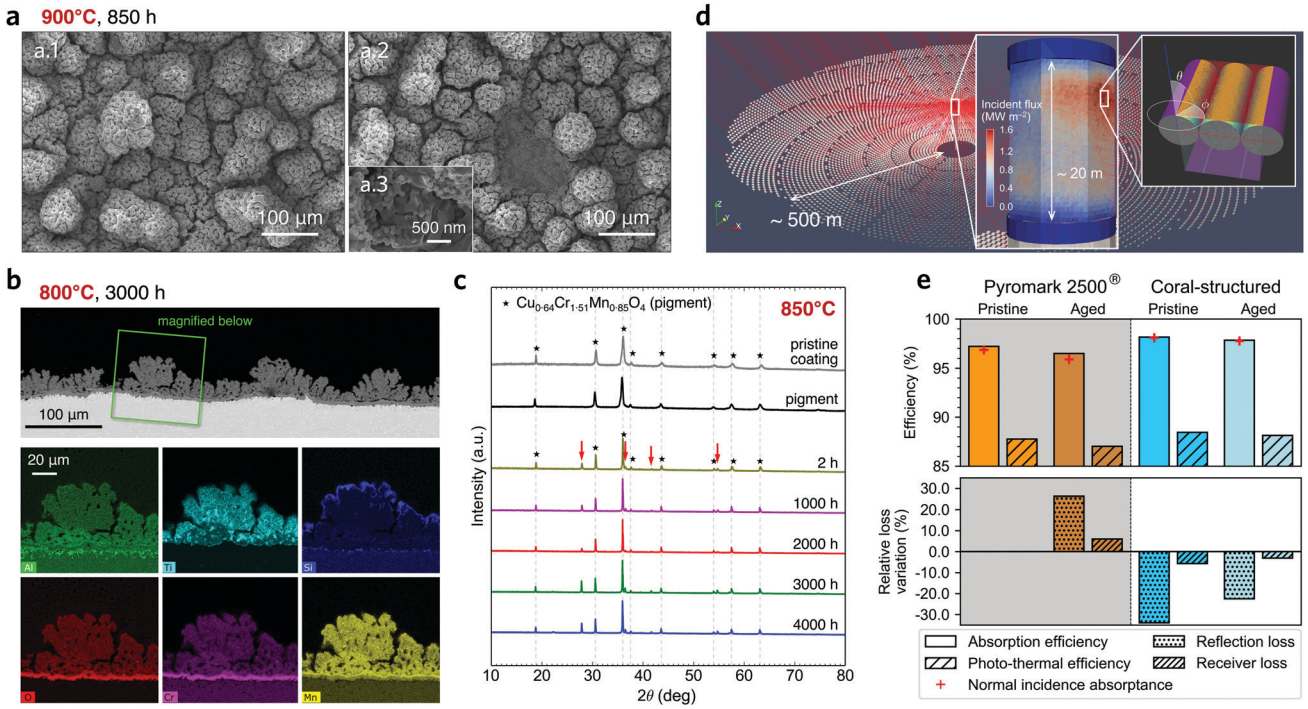

Fig. 4 Degradation and performance analysis after isothermal annealing. (a) SEM images after annealing at 900 °C for 850 h; the higher temperature promotes thicker cracks, but the coral morphology was largely maintained (a.1) with occasional peeling off in discrete locations (a.2); the nano-scale morphology brought by the nanospheres (a.3) was largely unaltered. (b) Cross-section BSE image and elemental mapping of the coral-structured coating after 3000 h at 800 °C; the coral-structured morphology largely unchanged, with a formation of a substrate-protecting chromium oxide layer underneath the coating (details in Note 3, ESI†). (c) X-ray diffractometry patterns show minor changes in crystal phase structure after annealing. The patterns for the pigment are indicated with stars. Rutile TiO_2 crystalises after heat treatment at 850 °C for 2 h, as indicated with red arrows. (d) Monte Carlo ray-tracing simulations of a 100 MW_{th} central tower CST plant; the rightmost inset shows the model used to determine the optical properties of tube banks (details in Note 6, ESI†). (e) Efficiency of light absorption and overall photo-thermal efficiency of the receiver with the Pyromark 2500® coating and our coating, before and after ageing for 1000 h at 800 °C (selected because Pyromark does not fail). Relative loss variation in the lower plot is measured relative to the pristine Pyromark efficiency results.

(Fig. S18, ESI†) and did not degrade significantly. Importantly, on-sun testing and laboratory-based experiments yielded similar spectral absorptance results (Fig. S18e, ESI†).

It is worth noting that, although the surface area of the coating is increased to a large extent by the hierarchical structure (compared to conventional rather flat coatings such as Pyromark), the net heat loss does not increase proportional to the surface area. For radiative heat loss, the aperture area is independent of the coating roughness while the thermal loss may increase with a large emittance caused by the cavity effect of hierarchical features (*i.e.* closer to the blackbody behaviour). For turbulent convective heat loss, the hierarchical features are expected to be submerged in the viscous sublayer so the surface appears smooth to the flow.[48] Even if the macro-scale features are larger than the viscous sublayer, pockets of hot air can be generated between macro-scale protrusions, as in the bladed solar thermal receiver of ref. 49, yielding a reduction in convective heat transfer.

Scalability for commercial solar thermal receivers

In recent years, many solar absorbers have been developed without demonstration of the scalability of the deposition method.[13,15,23] Here, the scalability of the proposed coral-structured absorber coating is successfully demonstrated by applying it onto a 1.2 MW_{th} commercial receiver[32] of *ca.* 2.9 m^2 (Fig. 1d inset; Fig. S24, ESI†): the solar-weighted absorptance and coating morphology are consistent with samples prepared in the laboratory. The absorption layer deposition process can be challenging due to the large amount of evaporated solvent, which is both hazardous and effective in cooling the receiver surface below the temperatures required to achieve a pyrolytic reaction.

A full-scale ray-tracing simulation of a CST power plant (Fig. 4d, Note 6, ESI†) is carried out to estimate the relative improvement of using the coral-structured coating compared to Pyromark. The modelling considers the solar irradiation reflected by the entire heliostat field, breaking down the absorbed energy by angle of incidence. Importantly, the tubular geometry on the surface of the large-scale cylindrical receiver is also considered. This tubular geometry acts as an additional macro-scale light-trapping feature (Fig. 2a.5) that slightly increases the absorption efficiency. The photo-thermal efficiency includes convection and radiation losses,[43,49] the latter considering measured emittance values (Fig. 3d). The results show that in pristine condition the coral-structured coating has a relative reduction in reflection loss of more than 30% in

comparison with Pyromark in its pristine state (Fig. 4e lower panel). The relative reduction in reflection loss becomes ~20% after 1000 h of ageing at 800 °C, whereas the aged Pyromark has an increase in the reflection losses from its pristine condition by ~25%. Hence, the proposed coating yields more than a 45% reduction (relative value) in reflection loss after ageing. These results confirm that the coral-structured coating significantly reduces reflection losses and improves optical resilience in a real solar thermal power plant.

Methods

Ray-tracing simulations for the coral morphology

The light absorption of various macro-scale stony-coral morphologies was simulated with TracePro, a Monte Carlo ray-tracing software. Monochromatic light was modelled with a uniform grid of source points on the rectangular upper boundary. Rays with normal incidence against the root mean square plane of the coral topography were emitted from each of the 40 000 source points. Before importing the scan of the coral morphology (Fig. 1c), a segment of the three-dimensional structure with a relatively small background curvature was selected (Fig. S1d–f, ESI†). The surface of the coral morphology was defined as an opaque and diffuse surface (Fig. 1c, vertical axis), with a constant absorptance on each surface element (same value as the flat surface; Fig. 1c, horizontal axis). To model the effect of the macro-scale morphology for highly absorbing surfaces, the flux threshold was set up to 0.0005 times the incident flux. The process of ray-tracing simulation was as follows: first, rays with equal power were emitted from the source. Then, each ray interacted with the coral surface and the total reflective power was computed. Parts of the secondary reflected rays intersected with the coral surface resulting in a re-absorption/re-reflection. This process continued until the ray energy reached the flux threshold. The overall absorptance α_{sim} value with macro-scale shown in Fig. 1c was calculated by

$$\alpha_{sim} = \frac{1 - E_{ref}}{E_{in}}, \quad (1)$$

where E_{ref} and E_{in} are the reflected and incident emissive powers, respectively. Ray-tracing simulations are a powerful tool to better understand light-trapping in animals, such as black birds[50] and corals (this study).

Ray-tracing simulations for the coral-structured coating

Monte Carlo ray-tracing simulations were conducted using two measurements as simulation inputs: (1) the macro-scale topography of the coating (inset of Fig. 3a), and (2) absorptance without the macro-scale morphology (Fig. 2c green solid line). A confocal microscope (SensoFar S Neox) was used to measure the coral-structured topography, which was then imported into the ray-tracing model to calculate the absorptance with macro-scale features (Fig. 2c, green dashed line) but still without nano-scale morphology. The absorptance without macro-scale features corresponded to the measured absorptance values of the base layer (Fig. 2c, blue solid line) because it has a similar micro-scale morphology (Fig. 1f). The simulation was conducted for wavelength intervals of $\Delta\lambda$ = 100 nm.

Effectiveness of morphological features

The effectiveness ε of a morphological feature in improving absorptance is defined as the percentage reduction of reflection loss with a surface having that morphological feature in comparison to the reflection loss by the flat surface. The effectiveness of a coral morphology is then written as

$$\varepsilon = 1 - \frac{1 - \alpha_{coral}}{1 - \alpha_{planar}}, \quad (2)$$

where α_{coral} and α_{planar} are the absorptance values of the macro-scale coral surface (Fig. 1c, vertical axis) and planar surface (Fig. 1c, horizontal axis), respectively. The effectiveness of each analysed coral morphology in Fig. 1c was found to be independent of the planar surface absorptance.

Materials preparation for the coral-structured coating

The proposed coating has three layers: base, absorption, and top layers, which required base, absorption, and top solutions, respectively. To prepare the base solution, an aluminium complex (aluminum ethylaceto acetate di iso-propirate) and isopropyl di glycol were mixed by screw stirring for 3 h. Black spinel pigments were then added and mixed by screw stirring for 12 h, at a weight ratio of *ca.* 1.15 : 1 of liquid to pigment ratio. To improve the adhesion with the metal substrate, a catalyst (*N*2-(aminoethyl)-3-aminopropyltrimethoxysilane) was then added and mixed with a screw stirrer for 3 h. The absorptance of twelve kinds of black spinels was measured before and after heat treatment (analysis for four promising pigments shown in Fig. S19 and S20, ESI†), resulting in the down selection of copper chromite manganese spinel, $Cu_{0.64}Cr_{1.51}Mn_{0.85}O_4$ (pigment size distribution in Fig. S21, ESI†). To prepare the absorption solution, a titanium precursor (titanium(IV) isopropoxide; TTIP) was first reacted with acetylacetone at room temperature, then heated at 80 °C for 6 h, and then diluted with 2-propanol (isopropyl alcohol, or IPA); the black pigments and *N*-methyl-2-pirrolidone were added and dispersed by ultra-sonication for 30 min. A large liquid solution to pigment ratio of *ca.* 40 : 1 is needed to produce the coral-structured morphology. To prepare the top solution, a tetraethyl orthosilicate mixture (mixture A) was added to a mixture with silica nanospheres reacted with a tetraethyl orthosilicate (mixture B) and then diluted with ethanol (Note 5, ESI†). In an attempt to improve the coating durability on a stainless steel 316L substrate, whose oxide layer peels off more easily than nickel-based alloys, an improved coating that had an additional primer layer (between substrate and base layer) was tested. The primer layer solution consisted of an aluminium complex diluted with IPA. The article reports improvement when using the substrate Inconel 625 and Haynes 230 (Fig. 3b and e), while the ESI,† provides durability results for stainless steels 316L (Fig. S12b, S13b and Note 4, ESI†). In an initial durability assessment,[51] we reported that the coral-structured coating with preliminary morphology was significantly durable on

stainless steel 253MA for ageing conditions at which Pyromark failed due to delamination.

Deposition method of the coral-structured coating

For laboratory-scale deposition, the coatings were sprayed under normal atmospheric conditions on 3 mm thick metallic coupons of 3 cm × 3 cm; deposition on cut tube samples was also conducted to test whether the coral-like morphology is kept when changing the substrate curvature. Inconel 625, Haynes 230, and stainless steels SS316L were used as substrate materials, as these are of interest to the CST industry. The underlying substrate was chemically cleaned and did not require grit blasting, as opposed to most reported coatings.[52] The Haynes 230 coupons was the only substrate type that was grit blasted (as in the Method "Preparation of benchmark Pyromark samples"). To deposit the base layer, the base solution was sprayed with a spraying nozzle twice while heating the substrate at 300 °C; the rapid evaporation of the solvent (iso propyl alcohol and isopropyl di glycol) produced the open micropore morphology observed for the base layer. To deposit the coral-structured absorption layer, the absorption solution was sprayed through a nozzle multiple times onto the base layer while it was held at *ca.* 300 °C. The thermal decomposition of titanium acetylacetonate complex, which only occurs when the substrate is held above 300 °C (acetylacetone desorbs from titanium acetylacetonate complex at *ca.* 300 °C), produced the coral-structured macro-scale morphology, while the rapid evaporation of the solvent (acetylacetone and IPA) produced the elongated micropores. Importantly, residual stresses at room temperature are expected since our coating forms at *ca.* 300 °C, potentially mitigating the large thermal stresses that occur at typical operating (ageing) temperatures. To deposit the top layer, the coupon was removed from the hotplate so that it cooled down to room temperature, and the top solution was then sprayed onto the absorption layer with an airbrush. Curing was conducted for 30 min at 400 °C after each spray pass of the top layer (two passes were conducted) to produce the 'pristine' samples.

To tune the self-assembled coral-structured morphology, several conditions need to be met. (**1**) *Adequate amount of acetylacetone to titanium precursor for proper coordination*; a large ratio of TTIP (wt%) to acetylacetone (AcAc, wt%) causes an excess of TiO_2, so a denser titanium bridged network with very few open micropores is created after the desorption process. On the other hand, when there is a small ratio of TTIP: AcAc, isolated TiO_2 is formed without the formation of a bridged network that can create the macro-scale protrusions, resulting in an absorption layer having only open micropores produced by the solvent evaporation (Fig. S14, ESI†). (**2**) *Stable substrate heating*; a substrate that can keep a temperature above 300 °C is needed to achieve the desorption of acetylacetone in the titanium acetylacetonate complex; the substrate temperature can be tuned to modify the number density of the macro-scale protrusions (Fig. S16, ESI†). (**3**) *Appropriate air and liquid pressures*; when spraying on the heated substrate, if the air pressure is much larger than that of the liquid, then the flow removes the coral-like protrusions before they adhere well to the base layer (Fig. S15, ESI†). (**4**) *Well-diluted absorption solution with IPA*; if the concentration of titanium is too large, then neither open micropores nor macro-scale coral-like protrusions appear. (**5**) *Distance from nozzle to substrate*; for an excessively short distance, the substrate becomes soaked preventing a quick solvent evaporation and resulting in a rather flat coating without macro-scale protrusions; for an excessively large distance, the protrusion size becomes small. These five conditions were modified to tune the micro- and macro-scale morphologies, *e.g.* increasing the protrusion size and number density (Fig. 3f), to improve the light absorptance of the coral-structured coating.

Preparation of benchmark Pyromark samples

Substrate coupons of stainless steel 316L, Inconel 625 (both 30 mm × 30 mm × 3 mm), and Haynes 230 (30 mm × 30 mm × 1 mm) were grit blasted using white aluminium oxide grit with mesh 60 (250 μm) at about 90 psi to remove any oxides and contaminations from the surface. Then, they were chemically cleaned by the following procedure: (**1**) soaking for 60 s in tetrachloroethylene, (**2**) scrubbing the surface for 30 s to remove any oils or contamination, (**3**) soaking for 60 s in methyl ethyl ketone, and (**4**) scrubbing them for 30 s.

Pyromark 2500 paint was applied using an Artlogic AC330 airbrush. The air pressure was adjusted at 50 psi and the airbrush gun was moved backward and forward over the coupon. This process is repeated eight times to achieve the target thickness (30–40 μm), which we found to perform well at 850 °C.[53] To have a uniform paint, in addition to keeping the gun about 10 cm above the samples, after each spray pass the surface was allowed to dry for ∼15 s before applying the following pass. Samples are then allowed to dry for 18–24 h before being cured. The curing process follows this process: (**1**) 120 °C for 2 h, (**2**) 250 °C for 2 h, (**3**) 540 °C for 1 h, (**4**) 750 °C for 1 h, and (**5**) cooled to the ambient temperature. It is worth noting that the Pyromark samples in this work exhibit higher initial absorptance than in a previously reported work[54] due to the presence of macro-scale cracks resulting from the modified deposition method described above.[52]

Absorptance measurement

To calculate the solar or solar-weighted absorptance (SWA, or α_{SW}) of the coatings, measurements of spectral absorptance $\alpha(\lambda)$ were carried out in the pristine state and after ageing, in the wavelength range of $\lambda = [250, 2500]$ nm. The SWA follows a clear consensus in the literature[16] defined as

$$\alpha_{SW} = \frac{\int_{280\,nm}^{2500\,nm} \alpha(\lambda) G(\lambda) d\lambda}{\int_{280\,nm}^{2500\,nm} G(\lambda) d\lambda}, \quad (3)$$

where $G(\lambda)$ is the standard G173-03 of the American Society for Testing and Materials (ASTM) for the spectral solar irradiance, commencing at λ = 280 nm; the upper limit of 2500 nm is deemed sufficient to capture most of the solar radiation. The spectral reflectance of the sample was measured at room

temperature by a spectrophotometer (PerkinElmer UV/VIS/NIR Lambda 1050) with an angle of incidence of 8°. The spectrophotometer was set to use an integrating sphere that measures the spectral directional–hemispherical reflectance ρ from the surface of the sample. As the samples are opaque, there is no transmittance and hence $\rho(\lambda) + \alpha(\lambda) = 1$, where ρ is the measured spectral hemispherical reflectance. The spectral values were measured with intervals of $\Delta\lambda$ =10 nm. A linear interpolation scheme was conducted to approximate the values of absorptance α at the wavelengths λ that were available in the reference solar irradiance spectrum G but not for the measurement α, which occurred in the lower wavelength range (where the resolution of G is $\Delta\lambda$ =0.5 nm). The approximated integrals in eqn (3) were evaluated at the same discrete values of λ. We found that using the interpolation scheme with the data obtained in intervals of $\Delta\lambda$ =10 nm yields the same results (up to three decimal places) as those obtained with the data having intervals of $\Delta\lambda$ = 5 nm.

It was found during the execution of the long-term isothermal ageing tests that the spectrophotometer produced slightly different measurements after each calibration (*e.g.* see solid lines in Fig. S22a, ESI†). The observed 'shift' in value was consistent with the accuracy of the instrument, which required a routine calibration. Importantly, we aimed at assessing optical resilience, *i.e.* relatively small change in absorptance relative to an initial value, by performing a highly precise measurement of the solar-weighted absorptance. Hence, the following correction for a more accurate relative measurement (dashed line in Fig. S22a, ESI†) was conducted for all wavelengths:

$$\rho_{\text{aged,corrected}} = \frac{\rho_{\text{benchmark,initial}}}{\rho_{\text{benchmark,measured}}} \times \rho_{\text{aged,measured}} \quad (4)$$

where $\rho_{\text{aged,corrected}}$ is the corrected reflectance (directional–hemispherical reflectance) of the aged sample, $\rho_{\text{benchmark,initial}}$ is the reflectance of a benchmark sample measured before ageing the sample, $\rho_{\text{benchmark,measured}}$ is the reflectance of the same benchmark sample measured when acquiring $\rho_{\text{aged,measured}}$, which is the measured reflectance of the aged sample (to be compared with the 'initial' sample before additional heat treatment). The benchmark sample is a preliminary coral-structured coating (*i.e.* before modifying macro-scale protrusions to improve absorptance, as in Fig. 3f) on Inconel 625 aged at 850 °C for 100 h. In addition, the repeatability of the measurement was excellent, within ±0.05% in the visible range and ±0.1% in the near infrared range (Fig. S22b, ESI†). The asymmetric error bar of the solar-weighted absorptance (Fig. 3b and e) was determined by the minimum and maximum values (lower and upper error bars, respectively) from a batch of samples aged in the same condition. For the long-term ageing, four to six samples were aged in each condition. A symmetric shaded region was used in the spectral absorptance measurement (Fig. 3a) and set to plus/minus one standard deviation.

The directional–hemispherical reflectance as a function of the angle of incidence (Fig. 2d and Fig. S8, ESI†) was measured with an add-on kit (Fig. S23a, ESI†), which provides manual control over the angle of incidence with an accuracy of 0.5°. The spectrophotometer is adjusted with a pinhole and lens so that the light can be narrowly focused on the centre of the sample to allow larger angles of incidence (up to ~82°). The light reflection profile (indicated in Fig. S23b, ESI†) is beyond the scope of this study.

Isothermal and thermal cycling ageing

The isothermal ageing was conducted in a programmable muffle furnace with small heating and cooling rates of 3 K min^{-1}, minimising possible effects of ramp rates. Hence, the time to reach the target temperature and return to room temperature at the end of the process was time additional to the ageing time. The thermal cycling ageing, both rapid cycling and cycle-and-hold patterns (ΔT = 200 K; see Fig. S9 and S10, ESI†), was conducted in an in-house apparatus comprising a split furnace assigned for heating at a given setpoint temperature and an airflow nozzle to cool the samples from the back of the substrate. Details of the experimental procedure can be found in our previous work.[18] For these measurements, additional thermocouples were inserted in the dummy sample to confirm that the temperature differences within the sample during the cooling process were small (<10 K) relative to the temperature difference within a cycle.

Materials characterisation

SEM characterisation of nano-, micro-, and macro-scale features (insets in Fig. 2a) was performed on a Zeiss UltraPlus analytical FESEM. A confocal microscope (SensoFar S Neox) was used for a quantitative measurement of the macro-scale topography (insets in Fig. 3a). XRD analysis was performed using a Bruker system (D2 Phaser, USA) equipped with Cu Kα radiation of average wavelength 1.54059 Å. EDX elemental mappings were performed on an FEI QEMSCAN. Samples were cut and mounted in epoxy resin for polishing. Next, the polished samples were carbon-coated prior to the elemental mapping.

Computational electromagnetics simulations

The magnitude and direction of the Poynting vector were analysed by Finite-Difference Time-Domain (FDTD) method using the software ANSYS Lumerical. A plane wave was launched from normal direction and then interacted with the top layer comprised of a matrix and nanospheres (Fig. S5c, ESI†). With an effective diameter of 124 nm and number density of 42 spheres per μm^2 obtained from SEM images, silica (SiO_2) nanospheres were placed randomly with 8 nm thickness SiO_2 matrix on top of the bulk material. The refractive indices of SiO_2 were obtained from literature.[55] To simulate the effect of nanospheres on top of a single material with similar initial wavelength-dependent absorptance as the coral-structured coating with micro- and macro-scales, we designed a dummy material with good light-absorbing properties (Fig. S5e, ESI†). Periodic boundary conditions were set in the lateral boundaries outside the randomly placed nanosphere distribution. A plane monitor collecting frequency-domain field profile and power was set, returning the Poynting vector and power

that were then normalised against the incident power (Fig. 2b top).

Scalability demonstration

A commercial liquid sodium receiver of Vast Solar (Fig. 1d inset) was used for these tests.[32] The heating of the receiver was conducted by circulating high-temperature oil that achieved a good surface temperature stability. The hazardous gases were removed using a doughnut-shaped exhaust around the spray (Fig. S24a, ESI†). The morphology and optical properties of the coating on the receiver agreed with those of samples prepared in a laboratory environment (Fig. S24b and c, ESI†).

Evaluation of the coating performance on a high-temperature receiver

The performance of the coatings considered in this study were numerically evaluated in a large-scale high-temperature CST system. The modelling of large-scale CST systems was performed using an in-house multi-physics modelling code in Python language coupled with radiative heat-transfer simulations. The complex geometrical optics interactions were solved using two open-source ray-tracing codes. Ray-tracing is computationally expensive when many geometrical elements are included in single simulations. Simulating a full-scale CST power plant is generally impractical because a conventional plant is comprised of tens of thousands of individually aimed heliostats onto receiver panels with detailed geometrical structures, such as pipe gaps and panel thermal insulation. Therefore, coating performance was made computationally tractable by splitting the global simulation into two steps addressing different length scales: Step (**1**) *simulations at the pipe length scale*, an elementary volume of receiver panel containing three adjacent pipes was used to determine the effective directional absorptance of coated pipes, and Step (**2**) *simulations at the CST power plant length scale*, the geometry of the receiver panels was approximated to planar apertures, placed tangent to the pipes. The directional absorptance of the coated pipes pre-determined in Step (**1**) was applied to the boundary surfaces in Step (**2**) to accurately determine the correct directional radiation absorption in each receiver panel.

Tracer,[56] to which the Australian National University is main contributor, is used for the pipe-level simulations in Step (**1**), while Solstice[57,58] from CNRS PROMES (Centre National de la Recherche Scientifique; Le Laboratoire PROcédés, Matériaux et Energie Solaire) is used for the heliostat field optics simulations in Step (**2**). See Note 6 (ESI†) for details on Steps (**1**) and (**2**).

Conclusions

Inspired by a stony-coral morphology that evolved over millions of years, we introduce a novel hierarchical structure with previously unexplored geometrical features in a high-temperature solar absorber coating. In its pristine condition, the coating has a solar-weighted absorptance $>98\%$ and an acceptance angle $>70^\circ$; in contrast, for Pyromark 2500 (state-of-the-art coating) with improved deposition these are 96% and 44°, respectively. This advancement yields a relative reduction in reflection loss of more than 30% in comparison with Pyromark in its pristine state when applied onto a large solar thermal receiver. Importantly, the cascaded light trapping in hierarchical features of our coral-structured coating produces a high-temperature light-absorbing structure with an outstanding optical stability and the highest solar-weighted absorptance of $97.75 \pm 0.04\%$ (average $\pm$ standard deviation) between 200 h and 2000 h of ageing at 850 °C. This sunlight absorption is the largest reported in the literature for a coating after thousands of hours of isothermal annealing at temperatures above 770 °C. This unmatched coating performance and durability is achieved through three innovations. First, the morphology of coral-like light-trapping structures is tuned *via* two distinct length-scale features: micro-scale holes of ~ 3 μm and macro-scale protrusions of >50 μm, which are produced through a combination of factors including thermal decomposition (Al and Ti) and solvent evaporation. Second, black spinel pigments are held together by highly dense oxide binders with reduced risk of coating delamination. Third, a top layer (comprised of silica nanospheres and a matrix) is applied on the external surface of the coral-structured coating to further increase the light absorption. Numerical simulations reveal the optical interactions in our coating and quantify the key role of its coral-inspired features in improving absorptance and optical resilience. Furthermore, the scalability of the coating is demonstrated on a commercial receiver in a pilot CST power plant, and ray-tracing simulations of a full-scale CST system indicate that the proposed coating reduces reflection losses by more than 45% in aged conditions with respect to the state-of-the-art. The proposed coating provides a significant innovation for CST technologies, paving the way for a durable and maintenance-free solar absorber coating.

Author contributions

Conceptualisation: J. F. T., K. T., Y. M., methodology: J. F. T., K. T., Y. M., K. D., investigation: J. F. T., K. T., Y. M., Y. G., S. H., C. A. A., M. T., A. T., W. L., J. C., visualisation: J. F. T., Y. G., S. H., C. A. A., M. T., funding acquisition: J. F. T., K. T., A. T., W. L., J. C., project administration: J. F. T., K. T., J. C., supervision: J. F. T., A. T., W. L., J. C., writing – original draft: J. F. T., C. A. A., J. C., writing – review & editing: J. F. T., K. T., Y. G., S. H., C. A. A., M. T., A. T., W. L., J. C.

Conflicts of interest

There are no conflicts to declare.

Acknowledgements

This research was supported by the Australian Research Council (ARC) Linkage Project (LP170101239) funded by the Australian Government, and the New Energy and Industrial Technology

Development Organization (NEDO) New Energy Venture Business Technology Innovation Program (P10020) funded by the Japanese Government. Funding from industry partners Vast Solar and Nano Frontier Technology is acknowledged. The microscope analysis was conducted in the Center of Advanced Microscopy (CAM) at the Australian National University node of the Microscopy Australia. The authors thank Dr Felipe Kremer and Dr Hua Chen for helpful discussion on microscopic imaging. Ms Nicole Blinco assisted with the scalability experiment; Dr Sonia C. Alvarez introduced different kinds of coral species. Their contribution is also acknowledged. The authors thank Dr Thomas P. White, Dr Yuerui Lu, and Dr Mona E. Mahani for their thoughtful feedback.

Notes and references

1 K. Frankowiak, X. T. Wang, D. M. Sigman, A. M. Gothmann, M. V. Kitahara, M. Mazur, A. Meibom and J. Stolarski, *Sci. Adv.*, 2016, **2**, 1–8.
2 D. Schlichter, H. W. Fricke and W. Weber, *Mar. Biol.*, 1986, **91**, 403–407.
3 L. Muscatine and J. W. Porter, *Bioscience*, 1977, **27**, 454–460.
4 K. J. A. Zawada, M. Dornelas and J. S. Madin, *Coral Reefs*, 2019, **38**, 1281–1292.
5 S. Enríquez, E. R. Méndez and R. Iglesias-Prieto, *Limnol. Ocean.*, 2005, **50**, 1025–1032.
6 N. S. Lewis, *Science*, 2016, **351**, aad1920.
7 D. Puig, M. Moner-Girona, D. M. Kammen, Y. Mulugetta, A. Marzouk, M. Jarrett, Y. Hailu and N. Nakićenović, *Science*, 2021, **373**, 616–619.
8 E. A. Fletcher and R. L. Moen, *Science*, 1977, **197**, 1050–1056.
9 C. K. Ho and B. D. Iverson, *Renewable Sustainable Energy Rev.*, 2014, **29**, 835–846.
10 W. Lipiński, E. Abbasi-Shavazi, J. Chen, J. Coventry, M. Hangi, S. Iyer, A. Kumar, L. Li, S. Li, J. Pye, J. F. Torres, B. Wang, Y. Wang and V. M. Wheeler, *Appl. Therm. Eng.*, 2021, **184**, 116137.
11 A. Henry, R. Prasher and A. Majumdar, *Nat. Energy*, 2020, **5**, 635–637.
12 K. Zhang, L. Hao, M. Du, J. Mi, J. N. Wang and J. Ping Meng, *Renewable Sustainable Energy Rev.*, 2017, **67**, 1282–1299.
13 L. Noč, E. Šest, G. Kapun, F. Ruiz-Zepeda, Y. Binyamin, F. Merzel and I. Jerman, *Energy Environ. Sci.*, 2019, **12**, 1679–1694.
14 C. K. Ho, A. R. Mahoney, A. Ambrosini, M. Bencomo, A. Hall and T. N. Lambert, *J. Sol. Energy Eng.*, 2014, **136**, 014502.
15 E. B. Rubin, Y. Chen and R. Chen, *Sol. Energy Mater. Sol. Cells*, 2019, **195**, 81–88.
16 S. Caron, J. Garrido, J. Ballestrín, F. Sutter, M. Röger and F. Manzano-Agugliaro, *Renewable Sustainable Energy Rev.*, 2022, **154**, 111818.
17 D. Xinkang, W. Cong, W. Tianmin, Z. Long, C. Buliang and R. Ning, *Thin Solid Films*, 2008, **516**, 3971–3977.
18 J. F. Torres, I. Ellis and J. Coventry, *Sol. Energy Mater. Sol. Cells*, 2020, **218**, 110719.
19 K. Cui and B. L. Wardle, *ACS Appl. Mater. Interfaces*, 2019, **11**, 35212–35220.
20 J. V. Anguita, M. Ahmad, S. Haq, J. Allam and S. R. P. Silva, *Sci. Adv.*, 2016, **2**, 1–9.
21 H. Y. Nan, Z. H. Ni, J. Wang, Z. Zafar, Z. X. Shi and Y. Y. Wang, *J. Raman Spectrosc.*, 2013, **44**, 1018–1021.
22 J. Moon, D. Lu, B. VanSaders, T. K. Kim, S. D. Kong, S. Jin, R. Chen and Z. Liu, *Nano Energy*, 2014, **8**, 238–246.
23 E. B. Rubin, S. Shin, Y. Chen and R. Chen, APL Mater.
24 I. E. Khodasevych, L. Wang, A. Mitchell and G. Rosengarten, *Adv. Opt. Mater.*, 2015, **3**, 852–881.
25 C. M. Lampert, *Sol. Energy Mater.*, 1979, **2**, 1–17.
26 J. Moon, T. K. Kim, B. VanSaders, C. Choi, Z. Liu, S. Jin and R. Chen, *Sol. Energy Mater. Sol. Cells*, 2015, **134**, 17–42.
27 T. K. Kim, B. VanSaders, E. Caldwell, S. Shin, Z. Liu, S. Jin and R. Chen, *Sol. Energy*, 2016, **132**, 257–266.
28 M. Bichotte, T. Kämpfe, W. Iff, F. Celle, S. Reynaud, T. Pouit, A. Soum-Glaude, A. Le Gal, L. Dubost and Y. Jourlin, *Sol. Energy Mater. Sol. Cells*, 2017, **160**, 328–334.
29 L. G. Radosevich, *Final report on the power production phase of the 10 MWe Solar Thermal Central Receiver Pilot Plant*, Sandia National Laboratories, Albuquerque, NM, 1988.
30 M. López-Herraiz, A. B. Fernández, N. Martinez and M. Gallas, *Sol. Energy Mater. Sol. Cells*, 2017, **159**, 66–72.
31 L. Noč and I. Jerman, *Sol. Energy Mater. Sol. Cells*, 2022, **238**, 111625.
32 J. Coventry, C. Andraka, J. Pye, M. Blanco and J. Fisher, *Sol. Energy*, 2015, **122**, 749–762.
33 M. Mehos, H. Price, R. Cable, D. Kearney, B. Kelly, G. Kolb and F. Morse, *Concentrating Solar Power Best Practices*, National Renewable Energy Laboratory, Golden, CO, 2020.
34 W. Wang, F. Ye, W. Mu, J. Dutta and B. Laumert, *ACS Appl. Mater. Interfaces*, 2021, **13**, 45008–45017.
35 S. Zeng, S. Pian, M. Su, Z. Wang, M. Wu, X. Liu, M. Chen, Y. Xiang, J. Wu, M. Zhang, Q. Cen, Y. Tang, X. Zhou, Z. Huang, R. Wang, A. Tunuhe, X. Sun, Z. Xia, M. Tian, M. Chen, X. Ma, L. Yang, J. Zhou, H. Zhou, Q. Yang, X. Li, Y. Ma and G. Tao, *Science*, 2021, **373**, 692–696.
36 J. Aizenberg, J. C. Weaver, M. S. Thanawala, V. C. Sundar, D. E. Morse and P. Fratzl, *Science*, 2005, **309**, 275–278.
37 X. Zhang, X. Shi, Y. Li, F. Wang and B. Lin, *Opt. Express*, 2021, **29**, 26669.
38 A. I. Kuznetsov, A. E. Miroshnichenko, M. L. Brongersma, Y. S. Kivshar and B. Luk'yanchuk, Science.
39 L. Cao, J. S. White, J. S. Park, J. A. Schuller, B. M. Clemens and M. L. Brongersma, *Nat. Mater.*, 2009, **8**, 643–647.
40 C. M. A. Parlett, K. Wilson and A. F. Lee, *Chem. Soc. Rev.*, 2013, **42**, 3876–3893.
41 S. Tang, W. Qiu, S. Xiao, Y. Tong and S. Yang, *Energy Environ. Sci.*, 2020, **13**, 660–684.
42 M. Fang, G. Dong, R. Wei and J. C. Ho, *Adv. Energy Mater.*, 2017, **7**, 1–25.
43 J. F. Torres, F. Ghanadi, I. Nock, M. Arjomandi and J. Pye, *Int. J. Heat Mass Transf.*, 2018, **119**, 418–432.
44 A. Boubault, B. Claudet, O. Faugeroux and G. Olalde, *Sol. Energy Mater. Sol. Cells*, 2014, **123**, 211–219.
45 G. Kang, H. Park, D. Shin, S. Baek, M. Choi, D. H. Yu, K. Kim and W. J. Padilla, *Adv. Mater.*, 2013, **25**, 2617–2623.

46 G. Cao, Z. Li, J. Tang, X. Sun and Z. Liu, *High Temp. Mater. Process.*, 2017, **36**, 927–935.
47 R. J. Bennett, R. Krakow, A. S. Eggeman, C. N. Jones, H. Murakami and C. M. F. Rae, *Acta Mater.*, 2015, **92**, 278–289.
48 D. Chung, N. Hutchins, M. P. Schultz and K. A. Flack, *Annu. Rev. Fluid Mech.*, 2021, **53**, 439–471.
49 J. F. Torres, F. Ghanadi, Y. Wang, M. Arjomandi and J. Pye, *Int. J. Heat Mass Transf.*, 2020, **147**, 118906.
50 D. E. McCoy, T. Feo, T. A. Harvey and R. O. Prum, *Nat. Commun.*, 2018, **9**, 1–8.
51 K. Tsuda, Y. Murakami, J. F. Torres and J. Coventry, *AIP Conf. Proc.*, 2018, **2033**, 040039.
52 A. Ambrosini, A. Boubault, C. K. Ho, L. Banh and J. R. Lewis, *AIP Conf. Proc.*, 2019, **2126**, 030002.
53 J. Coventry and P. Burge, *AIP Conf. Proc.*, 2017, **1850**, 030012.
54 C. K. Ho, A. R. Mahoney, A. Ambrosini, M. Bencomo, A. Hall and T. N. Lambert, *Proceedings of the ASME 2012 6th International Conference on Energy Sustainability*, San Diego, USA, 2012, p. 91374.
55 L. Gao, F. Lemarchand and M. Lequime, *Opt. Express*, 2012, **20**, 15734.
56 C.-A. Asselineau, Tracer: a Pythonic ray-tracing package with solar energy focus, https://github.com/casselineau/Tracer.
57 Solstice: The solar plant simulation tool, https://www.meso-star.com/projects/solstice/solstice.html.
58 Y. Wang, D. Potter, C. A. Asselineau, C. Corsi, M. Wagner, C. Caliot, B. Piaud, M. Blanco, J. S. Kim and J. Pye, *Sol. Energy*, 2020, **195**, 461–474.

